Key Points:
- Lithosphere beneath Tristan is 65–70 km thick; the low-velocity zone below shows V_S of 4.1–4.2 km/s
- Mantle potential temperature that fits surface wave and other data is 1,410–1,430°C
- The high mantle temperature is consistent with a plume origin of volcanism, but it is lower than beneath Hawaii

Correspondence to:
R. Bonadio,
bonadio@cp.dias.ie

Hot Upper Mantle Beneath the Tristan da Cunha Hotspot From Probabilistic Rayleigh-Wave Inversion and Petrological Modeling

Raffaele Bonadio[1] [ID], **Wolfram H. Geissler[2]** [ID], **Sergei Lebedev[1]** [ID], **Javier Fullea[1]** [ID], **Matteo Ravenna[1]** [ID], **Nicolas L. Celli[1]** [ID], **Wilfried Jokat[2,3]** [ID], **Marion Jegen[4]** [ID], **Christoph Sens-Schönfelder[5]** [ID], and **Kiyoshi Baba[6]** [ID]

[1]School of Cosmic Physics, Geophysics Section, Dublin Institute for Advanced Studies, Dublin, Ireland, [2]Alfred Wegener Institute, Helmholtz Centre for Polar Research, Bremerhaven, Germany, [3]Department of Geosciences, University of Bremen, Bremen, Germany, [4]GEOMAR, Helmholtz Centre of Ocean Research Kiel, Kiel, Germany, [5]Helmholtz-Zentrum Potsdam Deutsches Geoforschungszentrum, Potsdam, Germany, [6]Earthquake Research Institute, University of Tokyo, Tokyo, Japan

Abstract Understanding the enigmatic intraplate volcanism in the Tristan da Cunha region requires knowledge of the temperature of the lithosphere and asthenosphere beneath it. We measured phase-velocity curves of Rayleigh waves using cross-correlation of teleseismic seismograms from an array of ocean-bottom seismometers around Tristan, constrained a region-average, shear-velocity structure, and inferred the temperature of the lithosphere and asthenosphere beneath the hotspot. The ocean-bottom data set presented some challenges, which required data-processing and measurement approaches different from those tuned for land-based arrays of stations. Having derived a robust, phase-velocity curve for the Tristan area, we inverted it for a shear wave velocity profile using a probabilistic (Markov chain Monte Carlo) approach. The model shows a pronounced low-velocity anomaly from 70 to at least 120 km depth. V_S in the low velocity zone is 4.1–4.2 km/s, not as low as reported for Hawaii (~4.0 km/s), which probably indicates a less pronounced thermal anomaly and, possibly, less partial melting. Petrological modeling shows that the seismic and bathymetry data are consistent with a moderately hot mantle (mantle potential temperature of 1,410–1,430°C, an excess of about 50–120°C compared to the global average) and a melt fraction smaller than 1%. Both purely seismic inversions and petrological modeling indicate a lithospheric thickness of 65–70 km, consistent with recent estimates from receiver functions. The presence of warmer-than-average asthenosphere beneath Tristan is consistent with a hot upwelling (plume) from the deep mantle. However, the excess temperature we determine is smaller than that reported for some other major hotspots, in particular Hawaii.

Plain Language Summary The chains of volcanic ocean islands such as Hawaii are created when oceanic tectonic plates move over anomalously hot regions (hotspots) in the underlying mantle. The origin of hotspots has been attributed to mantle plumes, spectacular hot upwellings from the Earth's core-mantle boundary (2,800 km depth). The existence of the plumes and their occurrence beneath particular locations of volcanism are a matter of a heated debate. One way to find out whether a hot upwelling may be present is to determine the temperature in the mantle at depths just beneath the tectonic plate in the location of a hotspot. These depths are around 100 km, however, and temperature there cannot be measured directly. In this study, we used new seismic data from an array of ocean-bottom seismometers deployed around Tristan da Cunha, a prominent hotspot in the South Atlantic Ocean, and determined seismic velocities beneath it. Seismic velocities depend on the temperature of the mantle rock. We were able to use this dependence to infer the temperature within and below the tectonic plate around Tristan. The temperature is anomalously high. This is consistent with a hot mantle plume reaching Tristan from below and causing the unusual, long-lived volcanism at this location.

1. Introduction

Tristan da Cunha (TdC) is a hotspot in the South Atlantic Ocean, located ~450 km east of the Mid-Atlantic Ridge (MAR) (Figure 1a). The intraplate volcanoes and seamounts that form the TdC archipelago are connected to the
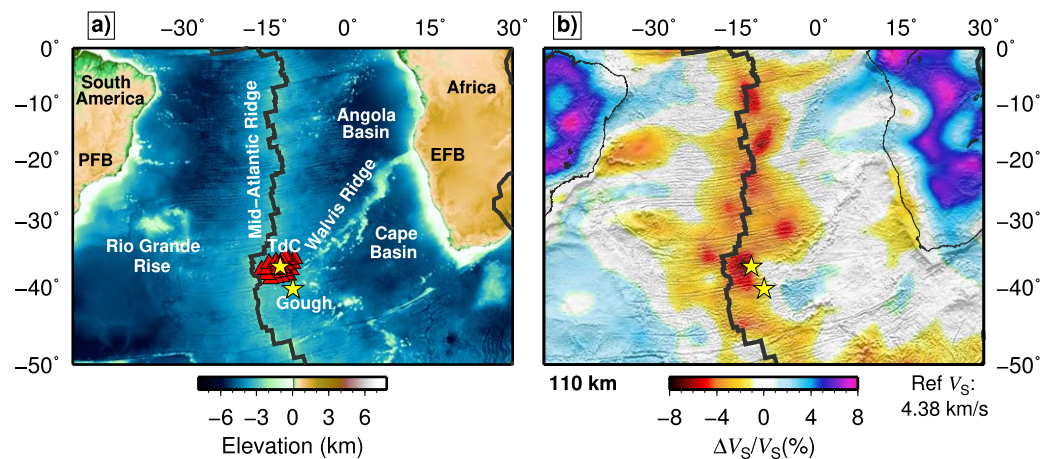
Figure 1. (a) Topographic map of the South Atlantic region. The seismic stations deployed in the vicinity of the Tristan da Cunha (TdC) hotspot are shown with red triangles. The TdC hotspot (the yellow star over the triangles) is located ~450 km east of the MAR, at the southwestern extremity of the Walvis Ridge. (b) Shear wave speed anomalies at 110 km depth beneath the South Atlantic region, according to waveform tomography of Celli et al. (2016). The two stars indicate the position of the TdC and Gough hotspots. A strong low V_S anomaly is located between TdC and the MAR. Topography and bathymetry are from the GINA (Lindquist et al., 2004) and ETOPO2 (NOAA, 2006) data sets.

Cretaceous (~132 Ma) Etendeka continental flood basalt province in Namibia via the aseismic Walvis Ridge. The ridge is built-up by seamounts and submarine volcanic plateaus that show a clear age progression and extend from the Namibian continental margin (northeast) to the volcanic islands of TdC and Gough (southwest), surrounded by 10–30 m.y. old lithosphere. Age-progressive distribution of volcanic rock samples collected from the Walvis Ridge and the Rio Grande Rise west of the Mid-Atlantic Ridge provide evidence for the volcanism at TdC and the formation of the flood basalts in Namibia and Brazil to be due to a common hotspot source, with the Walvis Ridge and the Rio Grande Rise being the hotspot tracks (e.g., O'Connor & Duncan, 1990).

The origin of the TdC hotspot volcanism is debated, with competing hypothesis suggested. The TdC-Walvis Ridge system is one of the few examples of a complete hotspot track, and thus the TdC is believed by many workers to be a surface expression of an underlying mantle plume (e.g., Morgan, 1971, 1997). The hypothesis of a deep mantle plume origin of the hotspot volcanism at the TdC archipelago is supported by anomalous geochemical data and geochronological constraints (REE inversions, ^{40}Ar/^{39}Ar geochronology and geochemistry of alkaline igneous rocks, chemical zonation, petrological, and geochemical variations along the hotspot track) (e.g., Gibson et al., 2006; Humphris et al., 1985; Rohde et al., 2013a, 2013b) and global tomography; Courtillot et al. (2003) define TdC plume as "primary," French and Romanowicz (2015) classify TdC as "clearly resolved" plume.

Alternative explanations for the hotspot volcanism at and around TdC include convective processes in the shallow mantle, possibly a consequence of the South Atlantic opening, and faulting and fracturing of the oceanic lithosphere (e.g., Anderson, 2005; Fairhead & Wilson, 2005; Foulger & Natland, 2003). Other models (e.g., O'Connor et al., 2012; O'Connor & Jokat, 2015), while adopting the idea of a deep-sourced mantle plume, emphasize the relative motion between the African plate and the Tristan-Gough mantle plume since the opening of the South Atlantic. It has also been suggested that the origin of TdC could be controlled by the interaction between the African superplume and surrounding depleted mantle (Rohde et al., 2013b), or by the interaction of a plume with the MAR (e.g., Gassmöller et al., 2016).

Until recently, the seismic-station coverage of the South Atlantic, including the TdC region, was very sparse. Regional shear wave velocity (V_S) models derived from global observations of surface and shear waves (Figure 1b) show an anomalous region with low upper mantle velocities close to TdC (e.g., Celli et al., 2016; Schaeffer & Lebedev, 2013; Zhang & Tanimoto, 1993), generally consistent with the hotspot volcanism there being due to anomalously hot asthenosphere, brought about by a mantle plume. However, the large-scale models are characterized by strong lateral averaging in the region and cannot be used to determine the thermal structure of the lithosphere and asthenosphere beneath TdC and its immediate surroundings.

In 2012–2013, an amphibian seismological and electromagnetic experiment was carried out in the vicinity of the archipelago (section 2.1), with the goal of recording regional data that could provide insights into the regional-scale structure of the upper mantle beneath the area. The new data have already been used in a number of studies, including receiver-function analysis (Geissler et al., 2016), petrological analysis (Weit et al., 2016), magnetotelluric imaging (Baba et al., 2017), P wave tomography (Schlömer et al., 2017) and ambient-noise tomography (Ryberg et al., 2017). Intriguingly, the inferences from these studies differed. Schlömer et al. (2017) reported evidence for an underlying plume, imaging a low P wave velocity conduit within the upper mantle, which could be regarded as the top part of a weak mantle plume. Geissler et al. (2016) measured the thicknesses of the crust, lithosphere, and mantle transition zone using receiver functions and found no clear indications for the presence of a plume. Weit et al. (2016) investigated melt generation and magma transport and storage beneath TdC, using thermobarometric measurements, and inferred a mantle potential temperature (T_P) of $\sim$1,360°C for the TdC hotspot; the models proposed were consistent with a hot upwelling column with its base at around 90 km and its top at around 60 km. Baba et al. (2017) investigated the electrical conductivity structure of the upper mantle beneath TdC and did not find evidence of a distinct plume-like conductor beneath the area.

Key outstanding questions thus remain: is the asthenosphere beneath TdC anomalously hot, which it should be if the intraplate volcanism is caused by a hot upwelling (plume) from the deep mantle? Is the asthenosphere as hot as beneath recognized major hotspots, such as Hawaii? Are the thermal structure and thickness of the lithosphere beneath TdC anomalous and how do they compare to those beneath other major hotspots?

More observational evidence on the structure of the lithosphere-asthenosphere system beneath TdC is required to answer these questions and, ultimately, establish the origin of the TdC hotspot. In this paper, we measure phase velocities of Rayleigh surface waves using the data recorded by the ocean-bottom seismometer (OBS) array (section 2.2) and invert them for the V_S distribution with depth using a probabilistic approach (section 3). The V_S structure is sensitive to temperature and composition and yields new constraints on the thickness of the oceanic lithosphere and temperature within the asthenosphere. To verify and quantify our results further, we use computational petrological modeling (section 4) and derive estimates of the mantle potential temperature, melt content in the asthenosphere and the thickness of the lithosphere beneath TdC.

2. Data and Measurements

Cross-correlation of seismograms from pairs of stations can produce measurements of the fundamental-mode phase velocities in a very broad period range (e.g., Meier et al., 2004; Roux et al., 2011; Soomro et al., 2016), sufficient to constrain V_S structure in the entire lithosphere-asthenosphere depth range (e.g., Lebedev et al., 2006; Ravenna & Lebedev, 2018). Our ocean-bottom data set, however, presented a number of challenges: low signal-to-noise ratios, low data redundancy due to the short term of the deployment and its remoteness from areas of abundant seismicity, and the (nominal) 60 s period limit of the wide-band instruments. This required development of data-processing and measurement approaches different from those tuned for land-based arrays of stations. Applying these to our data, we assembled a large number of carefully selected phase-velocity measurements, and derived a robust phase-velocity curve that averaged across the TdC area.

2.1. Data/Experiment

Twenty-four OBS from the German DEPAS pool (Deutscher Geräte-Pool für Amphibische Seismologie) and 26 ocean-bottom magnetotelluric stations from GEOMAR Kiel and the University of Tokyo were deployed around the archipelago of TdC (Geissler, 2014) (Figure 2). The 24 OBS were equipped with Güralp CMG-40T broadband seismometers (60 s). The network also included two land stations (installed on Nightingale Island, southwest of the main island), each of which was equipped with a Guralp-3ESP seismometer (60 s). One of the stations (NIG01, Figure 2b) recorded earthquake data for the entire year, whereas the second station failed after a few days due to water damage. Unfortunately, the permanent station TRIS also recorded very little data from the early 2012 until the end of this experiment. Because the internal clocks of the OBS work independently for the duration of the experiment, the drifts of the clocks have to be measured by GPS synchronization before deployment and after recovery of the instruments. In two cases, the second
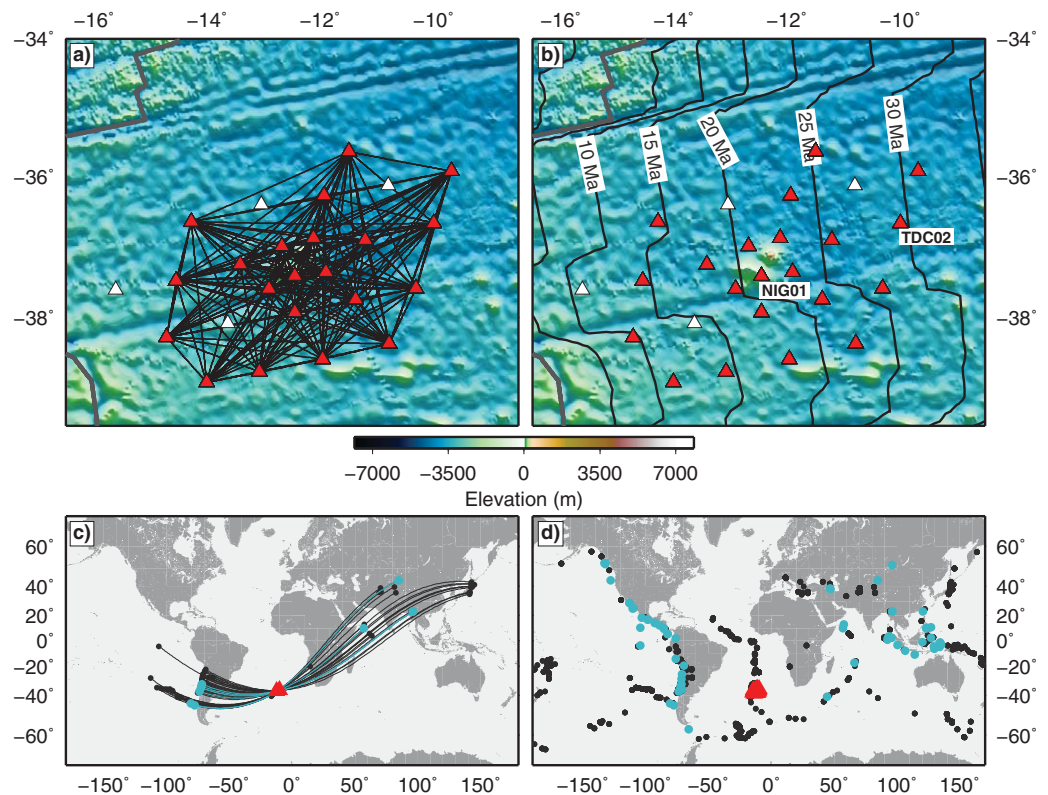
Figure 2. (a) Station locations (triangles) and interstation path coverage (black lines) yielded by our measurements. White triangles are stations with no data available. (b) Seismic stations and the seafloor age. The highlighted stations NIG01 and TDC02 are used in the following to illustrate the measurements (Figures 3 and 4). (c) Distribution of the events used to measure phase-velocity curves with the two-station method for the NIG01-TDC02 station pair; blue dots represent the events producing accepted measurements, out of all the events considered (blue and black). (d) Distribution of the events used to measure phase-velocity curves with the two-station method for all the pairs; blue dots represent the events used for the final set of accepted measurements. Topography and bathymetry are from the GINA (Lindquist et al., 2004) and ETOPO2 (NOAA, 2006) data sets.

synchronization failed. We thus used the noise-correlation approach (Sens-Schönfelder, 2008) to estimate the clock drift for these two instruments. The data were then corrected for the 2012 leap second, quality-checked and response-corrected to displacement. Tilt and compliance corrections were not performed on the data, given that, ultimately, we used only vertical-component signal at intermediate periods.

2.2. Measurements

Phase velocities were measured using a powerful recent implementation of the interstation cross-correlation method (Meier et al., 2004; Soomro et al., 2016). For each pair of stations within the array, phase velocities of the fundamental Rayleigh mode were calculated by means of cross-correlation of the waveforms of teleseismic earthquake recordings.

In this implementation of the two-station method, the cross-correlation function is filtered with a frequency-dependent Gaussian bandpass filter, and then it is windowed in the time domain with a frequency-dependent Gaussian window centered on the maximum amplitude of the cross-correlation function. Parts of the cross-correlation signal likely to be due to noise or correlation between the fundamental mode and other parts of the waveform (body waves and surface wave coda) are down-weighted (an example of phase-velocity measurement is shown in Figure 3). The resulting signal is transformed into the frequency domain and the phase is computed as the arctangent of the ratio of the imaginary to real part of the Fourier spectrum (Meier et al., 2004).

We performed our measurements using events from the Global Centroid Moment Tensor catalog (Dziewonski et al., 1981; Ekström et al., 2012). We chose the events with back-azimuth within 20° from the station-
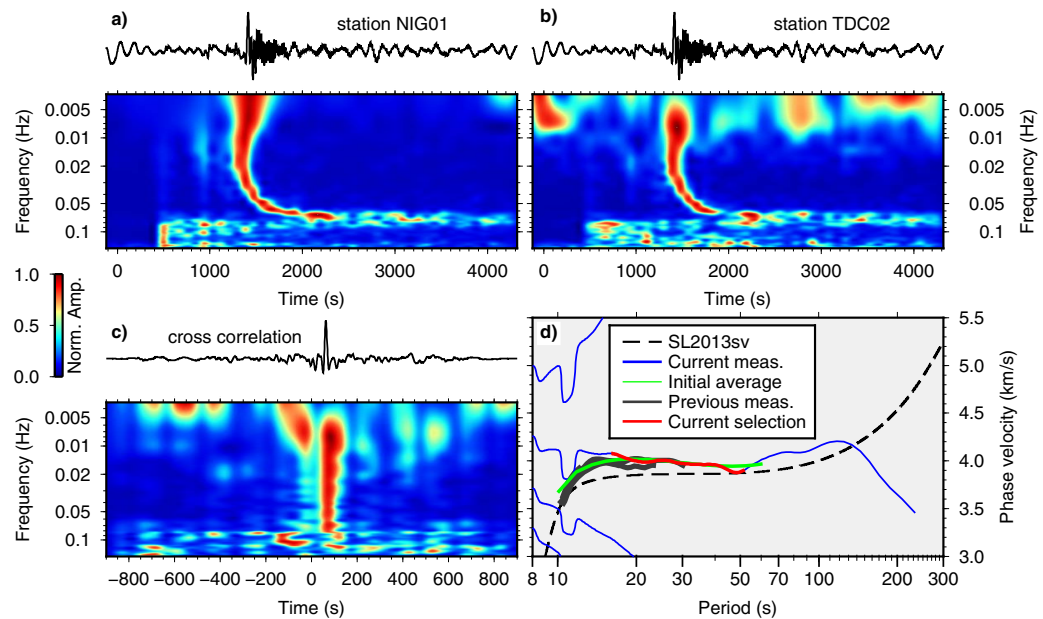
Figure 3. Example of an interstation, Rayleigh-wave, phase-velocity measurement for the station pair NIG01 (land) and TDC02 (ocean-bottom) (Figure 2b). (a and b) The recorded seismograms and the time-frequency representations of their waveforms. (c) The cross-correlation function and its time-frequency representation. (d) Phase-velocity curves (in blue, including alternative curves resulting from the 2π ambiguity) plotted together with the reference curve extracted from the global tomographic model SL2013sv (Schaeffer & Lebedev, 2013) (dashed black line). The current accepted segment is shown in red, previous measurements accepted for the current pair are shown in dark gray, initial average (computed from the distribution density plot, Figure 5) used as the regional reference model is shown in green.

station great circle path (GCP) and with a moment magnitude greater than 4.9, using a distance-dependent magnitude threshold as described in Schaeffer and Lebedev (2013). Phase velocities were computed from the phase of the cross-correlation function and the difference between the distances from the event to each of the stations (hence, the imperfect alignment of the two stations and the event had no immediate effect on the measurement accuracy).

The high noise level and the limited amount of usable ocean-bottom data necessitated careful, manual selection of acceptable phase-velocity measurements for each event. During the interactive measurement procedure, only smooth portions of phase-velocity curves were accepted. The criteria used for the selection were based on (1) the smoothness of the dispersion curve, (2) reasonable closeness to the reference model (exclusion of the outlier measurements), (3) the length of the selected segments (very short segments were not accepted), (4) the difference between measurements from events at opposite directions from the station pair (a systematic inconsistency—not encountered with measurements with this data set—could indicate instrumental errors or strong diffraction effects), and (5) the minimum number of measurements for each frequency (two measurements at least for each period) (Soomro et al., 2016). An example of the selection of dispersion curves for a pair of stations is shown in Figure 4.

The phase-velocity estimated from the cross-correlation function has to be compared with a reference model to eliminate the 2π ambiguity of the arctangent function and remove outlier measurements (Meier et al., 2004). (Figure 3d shows the array of possible phase-velocity curves estimated from the cross-correlation function in blue.) Initially, we tried out, as reference models, the Preliminary Reference Earth Model (PREM) (Dziewonski & Anderson, 1981), AK135 (Kennett et al., 1995), both models recomputed at a reference period of 50 s, and SL2013sv (Schaeffer & Lebedev, 2013) (as this is a three-dimensional model, for each pair of stations five points of the model grid along the path are used in the average, the two end points and three equally spaced points along the GCP). Neither of these turned out to be suitable, however, and a more accurate regional reference was required.

An accurate, representative reference model is essential in order to resolve the 2π ambiguity, especially at shorter periods, in the course of interactive phase-velocity measurements. We found a way to extract such
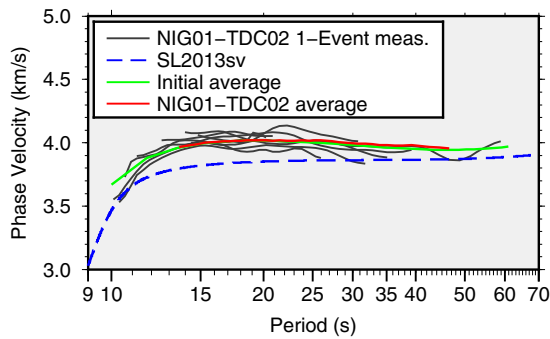
Figure 4. Results of the interactive, cross-correlation one-event measurements of phase-velocity curves for the station pair NIG01-TDC02 (dark gray lines). Reference curves shown are SL2013sv (computed from Schaeffer and Lebedev (2013)) and the average regional curve extracted from the distribution density plot (Figure 5).

an average regional curve from the data quickly. We ran the automated phase-velocity measurement routine of Soomro et al. (2016) with loose selection criteria and marked all event-station pair combinations for which a measurement was successful for any curve segment. (This initial preselection is necessary to remove random "measurements" from seismograms dominated by noise.) For all the selected signals, we summed all branches of the entire families of possible phase-velocity curves (with no attempt to resolve the 2π ambiguity) in the entire 8–250 s period range. This yielded a density distribution plot (Figure 5) with a stack of all the measurements in the broad period range. With measurements from different interstation pairs stacked together, the region-average dispersion curve emerges clearly, with the curves affected by 2π ambiguity canceling out. The stacking strategy for the extraction of a reference phase-velocity dispersion curve is somewhat similar to that applied to ambient-noise data by Rawlinson et al. (2014). The maximum values of the distribution at each period have been used to extract a dispersion curve that was inverted using a nonlinear Levenberg-Marquardt gradient search algorithm (e.g., Agius & Lebedev, 2013, 2014; Erduran et al., 2008; Lebedev et al., 2006; Meier et al., 2004) for a V_S profile. The synthetic phase-velocity curve computed for this profile (green line in Figure 5) represents an accurate regional reference model. The best-fitting synthetic is very similar to the simple stack but is smoother, as is appropriate for a reference model. Despite being computed using relatively noisy data, the density plot shown in Figure 5 not only yields a useful reference for the subsequent case-by-case selection, but also shows that the measurements from the OBS data set naturally provide mutually consistent information.

We measured interstation phase velocities in a period range from ∼8 to ∼250 s, but since the instruments have a corner period of 60 s, only a small number of measurements (from the largest events) were successful at periods above 60 s. In order to constrain the lithosphere-asthenosphere structure beneath the area, we selected the most accurate measurements from all station pairs and computed a region-average dispersion curve (Figure 6). Generally, all the single-measurement curves show similar features and almost all of them lie above the global reference curves and show phase velocities close to 4 km/s at periods above 12–15 s. The region-average curve was computed as a simple average of all the single-event measurements. It is the most robust and accurate in the period range 13.6–46.5 s. The curve in this range (Figure 6) was
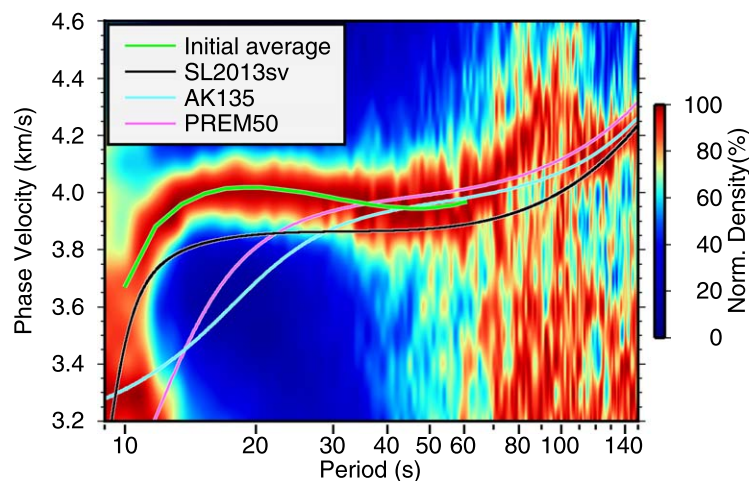
Figure 5. Density plot for the stack of automated preliminary measurements, normalized to the maximum at each period. The stack was computed using all branches of possible phase-velocity curves (including those affected by the 2π ambiguity), for all pairs of stations and for all automatically selected events. The average curve ("Initial average") determined from this distribution is shown in green. This regional reference is substantially different from those given by the global reference models AK135 (Kennett et al., 1995) and PREM50 (Dziewonski & Anderson, 1981) and from that extracted from the tomographic model SL2013sv (Schaeffer & Lebedev, 2013).
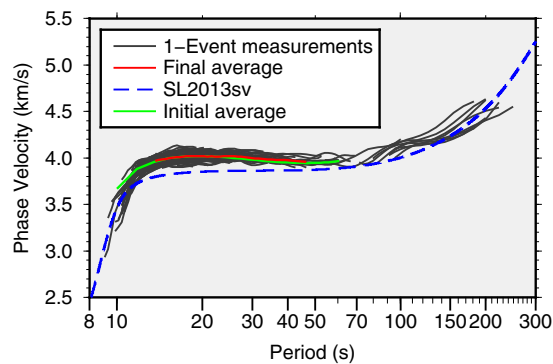
Figure 6. One-event dispersion measurements for all analyzed station pairs. The average phase-velocity curve (red line) is used for the 1-D inversion for V_S profile in depth. We limited the range of this curve to 13.6–46.5 s, where it is the smoothest, constrained by the most measurements and, therefore, the most accurate.

inverted for the 1-D V_S structure beneath the study area using a Markov chain Monte Carlo (McMC) algorithm (section 3).

Our average dispersion curve (Figure 6) shows a pronounced low-velocity anomaly at periods above 20 s. Comparing it to the Atlantic-average curves for 20–52 Ma lithospheric ages from James et al. (2014) (their Figure 5a), we observe that the curves show similar velocity values in the lithospheric range, while Tristan da Cunha average shows lower velocities at periods above 40 s (asthenospheric range). This indicates that the asthenosphere beneath Tristan is hotter than the Atlantic average for the Tristan-region lithospheric age. It is also useful to compare our phase velocities with those for the Indian Ocean from Godfrey et al. (2017); although the range of their overlap is narrow, we can see that the Indian Ocean dispersion curve for 20–52 Ma (green line in their Figure 3) and our average for Tristan da Cunha (e.g., Figure 6) are similar. The 20–52 Ma dispersion curve in Godfrey et al. (2017) is probably representative mostly of the eastern part of the Indian Ocean, with the spreading along the Southwest Indian Ridge much slower than that along the Southeast Indian Ridge and, thus, with the area from which the curves are computed greater in the eastern part of the ocean. The phase-velocity average for the Indian Ocean thus reflects the rejuvenation of the lithosphere by the Kerguelen hotspot (Godfrey et al., 2017; Schaeffer & Lebedev, 2015). Our phase velocities at periods over 40 s, sampling the low velocity zone, are around 4.0 km/s, not as low as the 3.9 km/s reported for the active volcanism part of Hawaii by Laske et al. (2011) (their Figure 4). By contrast, the Hawaii dispersion curve averaging along a path far from active volcanism (blue path in their Figure 4) shows velocities higher than in the Tristan da Cunha area.

We also inverted the interstation measurements from the various station pairs for phase-velocity maps (Deschamps et al., 2008; Lebedev & van der Hilst, 2008). The inversions showed that seismic-velocity heterogeneity in the area is relatively weak, which justified our use of a region-average profile to constrain the thermal structure of TdC. Because the lateral variations are relatively small and because the errors of the measurements are larger than in terrestrial studies using the same methods (e.g., Endrun et al., 2011; Pawlak et al., 2012; Polat et al., 2012), the variance reductions given by the tomographic inversions are relatively low (supporting information Figure S1). The maps do show interesting lateral variation in phase velocity; maps for different periods and for stacked period ranges (computed to highlight the dominant anomalies and reduce artifacts) are shown, for completeness, in supporting information Figures S1 and S2.

3. Probabilistic Inversion for an S-Velocity Profile

We inverted the average Rayleigh-wave, phase-velocity curve for the 1-D crustal and lithospheric V_{SV} (vertically polarized shear wave speed) structure using a Markov chain Monte Carlo (McMC) algorithm (Ravenna & Lebedev, 2018). The algorithm addresses the model nonuniqueness by directly sampling the parameter space in a Bayesian framework, providing a quantitative probabilistic measure of the solution space instead of a unique best-fitting model. The algorithm is also able to address the issue of data noise estimation by using a Hierarchical Bayesian approach (Bodin et al., 2012, 2016), which allows the variance of data noise to be treated as an unknown in the inversion (Ravenna & Lebedev, 2018).

Both the crustal and mantle structure were inverted for. The a priori information on the model parameters was expressed in terms of Gaussian prior probability distributions (characterized by standard deviations of approximately 400 m/s for the shear-velocity parameters and 2 km for the Moho depth) centered at values from the reference model. As a reference crustal model, we used a four-layered crustal model of the TdC region taken from CRUST 2.0 (Bassin et al., 2000), with a 3.4 km thick water layer and a Moho depth of 10.1 km. The reference model for the mantle is a modified version of AK135 (Kennett et al., 1995), characterized by constant shear velocities (4.45 km/s) until 220 km depth and linearly increasing shear velocities below 220 km depth. The sampled models were parameterized with 10 control points in the mantle (until 410 km depth) that represented the knots of piecewise cubic Hermite spline polynomials.
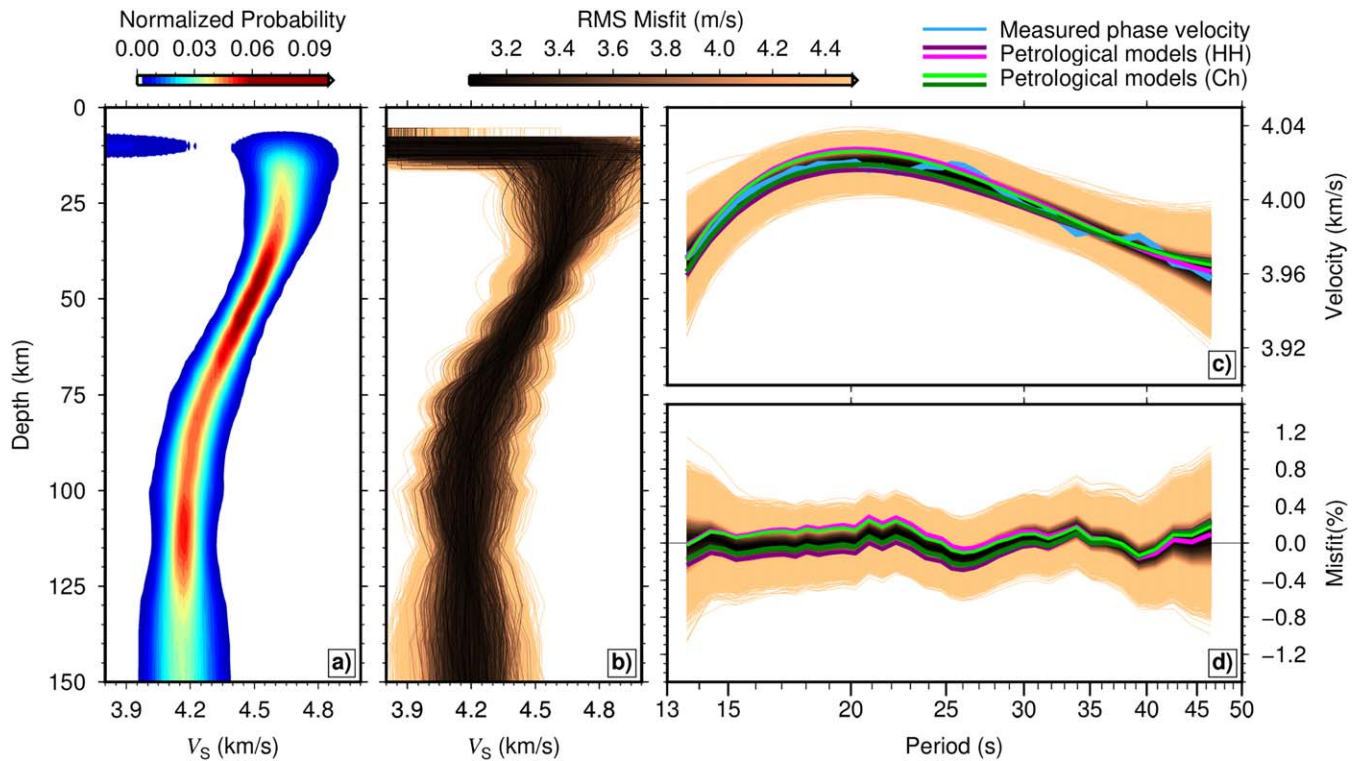
Figure 7. (a) The posterior distribution of the V_S profile with depth. (b) The models sampled in the McMC inversions. The posterior distribution comprises an ensemble obtained by merging the models sampled by four chains of iterations, each running independently. (c) The corresponding synthetic phase velocities. (d) The relative misfit relative to the measured data. All curves in Figures 7b, 7c, and 7d are colored according to the level of fit to the data. The light-blue line shows the measured phase velocities used in the inversions. The other curves show phase velocities computed for the petrological models described in section 4.

The posterior distribution of the V_S profile and the models sampled in the McMC inversions are shown in Figures 7a and 7b, respectively. The posterior distribution comprises an ensemble obtained by merging the models sampled by four chains of iterations running independently. The corresponding synthetic phase velocities and the relative misfit to the measured data are shown in Figures 7c and 7d, respectively.

Because of the limited period range of the data, we can expect it to constrain V_S structure down to somewhere in the shallow asthenosphere only. Figure 7a shows that the model is well constrained down to about 120 km depth and is uncertain below. The profile displays a clear contrast between the high-velocity lithosphere, with V_S up to 4.6–4.65 m/s, and a low-velocity asthenosphere, with V_S down to 4.1–4.2 m/s. The depth of the lithosphere-asthenosphere boundary can be estimated at around 65–70 km.

4. Petrologically Derived Models

Our inversion of phase velocities yields a probabilistic V_S profile and shows a range of models that fit the surface wave data. Only some of these models would be consistent with other available data, in particular the bathymetry in the region. We now take an approach alternative to the purely seismic inversion and use the integrated geophysical-petrological software LitMod (e.g., Afonso et al., 2008; Fullea et al., 2009) to estimate the thermal structure of the lithosphere-asthenosphere system consistent with both the seismic data and bathymetry. We compute a series of models of the lithosphere and the sublithospheric upper mantle and use them to estimate the range of values for the lithospheric thickness and the melt fraction and temperature of the asthenosphere beneath TdC.

The lithospheric geotherm is computed under the assumption of steady-state heat transfer in the lithospheric mantle, considering a P-T-dependent thermal conductivity in the mantle and prescribed thermal parameters in the crust. In the convecting sublithospheric mantle, the geotherm is given by an adiabatic
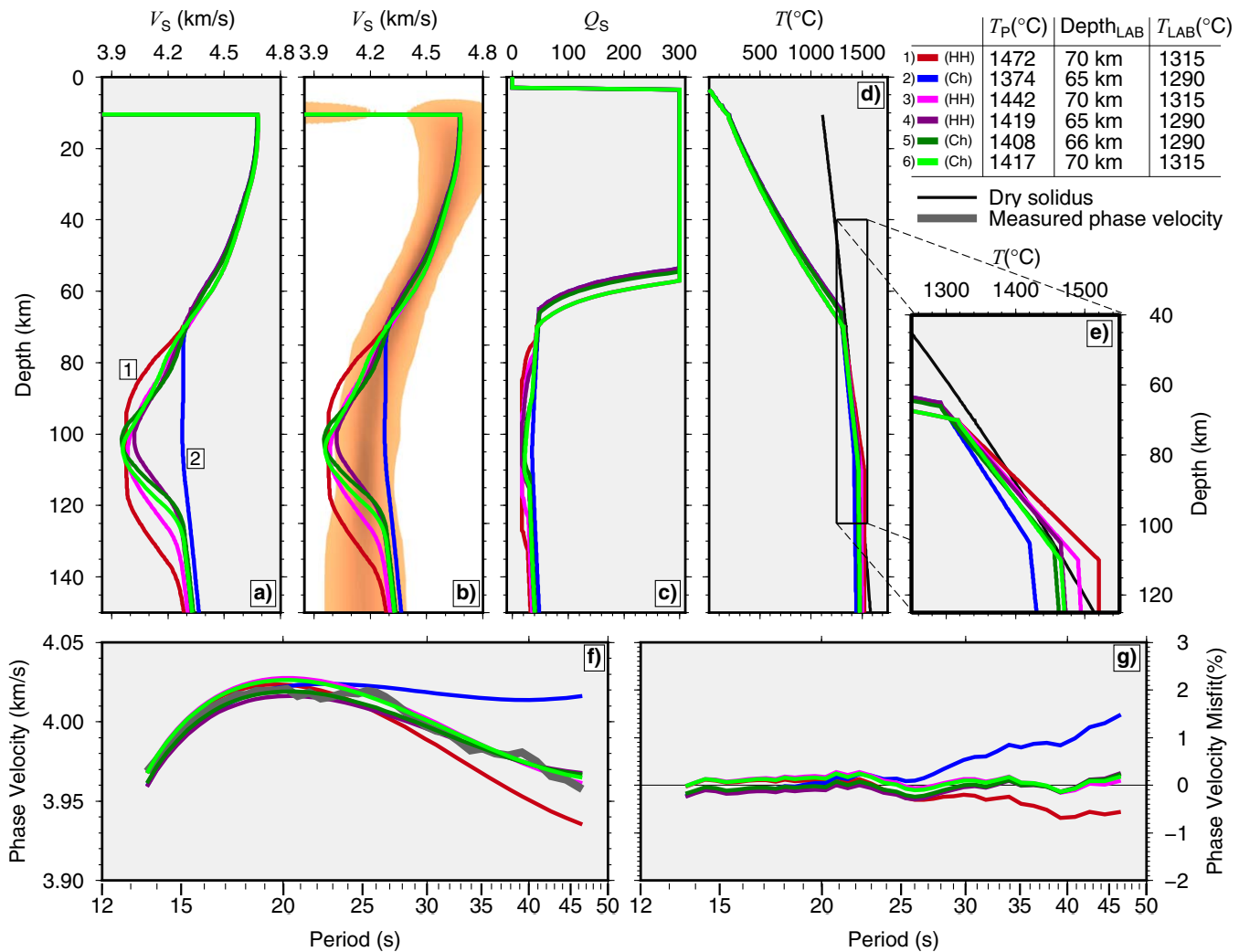
Figure 8. Six different petrological-geophysical models. Models 5 and 6 (dark and light green lines) and models 4 and 3 (dark and light purple lines) fit the data, whereas the other two models (1 and 2, red and blue lines, with the lowest and the highest V_S in the asthenosphere, respectively) do not. The key differences that set the models apart are the mantle potential temperature (T_P), LAB depth (Depth$_{LAB}$), and LAB temperature (T_{LAB}); the values for these parameters are listed in the legend, top right. (a and b) Shear velocity. The posterior distribution yielded by the purely seismic inversion is plotted in the background in Figure 8b. (c) Anelastic attenuation factor. (d) Temperature. (e) A zoom on the geotherms in the depth range comprising the LAB and the transitional layer beneath it. (f) Phase velocities. (g) Phase-velocity misfits yielded by the models. ~1% melt is present in model 1 from ~85 to ~140 km, in model 3 from ~88 to ~130 km, in model 4 from ~95 to ~122 km; $< \sim 0.5$% melt is present in model 5 from ~80 to ~117 km; melt is absent in models 2 and 6. "HH" and "Ch" indicate whether the model has been computed using, respectively, the parameterization by Hammond and Humphreys (2000a, 2000b) or Chantel et al. (2016).

temperature gradient. Between the lithosphere and the convecting sublithospheric mantle, we postulate a transitional buffer layer, characterized by a continuous linear superadiabatic gradient (i.e., heat transfer is controlled by both conduction and convection, see Fullea et al. (2009) for details). This linear superadiabatic gradient is controlled by the assumed temperature at the base of the lithosphere and sublithospheric mantle potential temperature. Stable mineral assemblages in the mantle are calculated using a Gibbs free energy minimization as described by Connolly (2005). Anharmonic seismic velocities are computed as a function of pressure, temperature, and bulk composition in the mantle as described in Fullea et al. (2012). Melt fractions are computed based on a mantle-peridotitic dry solidus and liquidus (Katz et al., 2003, and references therein). The effects of melt on V_S and V_P are computed according to the two experimental models: Hammond and Humphreys (2000a, 2000b) and Chantel et al. (2016) ("HH" and "Ch," respectively, in the legend in Figure 8).

Introducing melting into our models leads to discontinuous V_S and V_P decreases at the onset of even small fractions of melt (<1%). In line with experimental results suggesting a progressive, V_S-decreasing effect of

anelasticity below the solidus temperature (e.g., Takei, 2017; Yamauchi & Takei, 2016), we implement a linear parameterization to smooth the effect of melt on anharmonic seismic velocities over a temperature range in the vicinity of the solidus. We use a homologous temperature T_m defined as the temperature normalized to the solidus temperature (i.e., $T_m = 1$ at the solidus) and define a critical homologous temperature, T_{mc}, at which the anelasticity effects are introduced. Within the buffer range $T_{mc} < = T_m < 1$ the melt fraction varies linearly from zero at $T_m = T_{mc}$ to a threshold melt fraction at $T_m = 1$. (We emphasize that the gradient so defined does not represent actual melt but serves as a smoothing parameter, reflecting premelt effects on the rock aggregate anelastic behavior.) Slight further smoothing of the V_S profiles is performed using a sliding boxcar window with a 20 km half width. In all our models, we correct for anelastic attenuation effects as in Fullea et al. (2012) but we also include melt related variations in the seismic quality factor (Q) based on the laboratory results by Chantel et al. (2016). Surface elevation is modeled according to the local isostasy at lithospheric scale as described in Fullea et al. (2009). The assumed lithospheric mantle composition corresponds to an average oceanic peridotite (Fullea et al., 2015). For an exhaustive technical description of the geotherm construction and model calculation, we refer the reader to Fullea et al. (2012).

Six selected models with varying degrees of fit to the seismic data are presented in Figure 8, where we show the profiles of V_S, temperature and attenuation, as well as the observed and synthetic phase velocities and the phase-velocity misfit. Three key parameters of the models (given in the legend in the upper right corner) characterize the mantle geotherm: the mantle potential temperature T_P, the lithosphere-asthenosphere boundary (LAB) depth, and the temperature at the LAB.

Four of the models (models 3, 4, 5, and 6 in Figure 8), characterized by T_P in the 1,410–1,430°C range and the LAB depth of 65–70 km, fit the seismic data (Figures 8f, 8g and 7c, 7d), while also fitting the observed bathymetry (in the ~3,477–3,521 m range, compared to 3,452 ± 448 m the observed average across the region). The other two models (1 and 2, red and blue lines in Figures 8f and 8g) fit poorly and show that colder asthenosphere (lower T_P) (model 2, blue line) would result in synthetic phase velocities at the longer periods being much higher than the data; shallower or hotter LAB (model 1, red line) would result in phase velocities being lower than observed.

The well-fitting models are just four of the infinite number of similar models that would fit the data. The highly nonlinear effects of partial melting contribute to the nonuniqueness of the model.

The purely seismic and petrologically derived models are, overall, remarkably similar (Figure 8b). In the lithosphere, the V_S profiles show a very close agreement. In the shallow asthenosphere, the petrological models that yield V_S profiles at the edges of the Monte Carlo-derived distribution do not fit the data, and only the petrological models with V_S profiles within the distribution band do. The close agreement of the results of the two types of inversion and modeling (seismic and petrological) is important and validates our results.

The main difference between the different models is in the smoothness of the profiles in the upper asthenosphere. While surface wave data constrain V_S tightly in sufficiently broad depth ranges in the lithosphere and asthenosphere, they are not sensitive to the sharpness of discontinuities or narrow gradients (e.g., Bartzsch et al., 2011; Lebedev et al., 2013). Thus, the rough and the smooth models seen in Figure 8b can fit the data equally well. Even though the fine-scale structure of the V_S profile in the models is nonunique, they do confirm our inferences on the lithospheric thickness from purely seismic inversion and provide useful estimates of the mantle temperature (lithospheric and sublithospheric), while also demonstrating that the models are consistent with the observed bathymetry and heat flow.

5. Discussion

5.1. Comparison With Published V_S Profiles

In Figure 9, we compare our region-average V_S profile derived through McMC inversion with published V_S profiles for Hawaii (Laske et al., 2011), young Pacific lithosphere (Harmon et al., 2009; Nishimura & Forsyth, 1989) and the 10, 20, and 30 Ma profiles for the Pacific and South Atlantic Oceans from global waveform tomography (Celli et al., 2016).

The profiles of Laske et al. (2011) (Figure 9a) were obtained with similar data and methods to the ones used here, i.e., two-station dispersion measurements using data from an OBS array, with the interstation spacing in the two experiments comparable (the Hawaii OBS array, however, included more instruments, and they
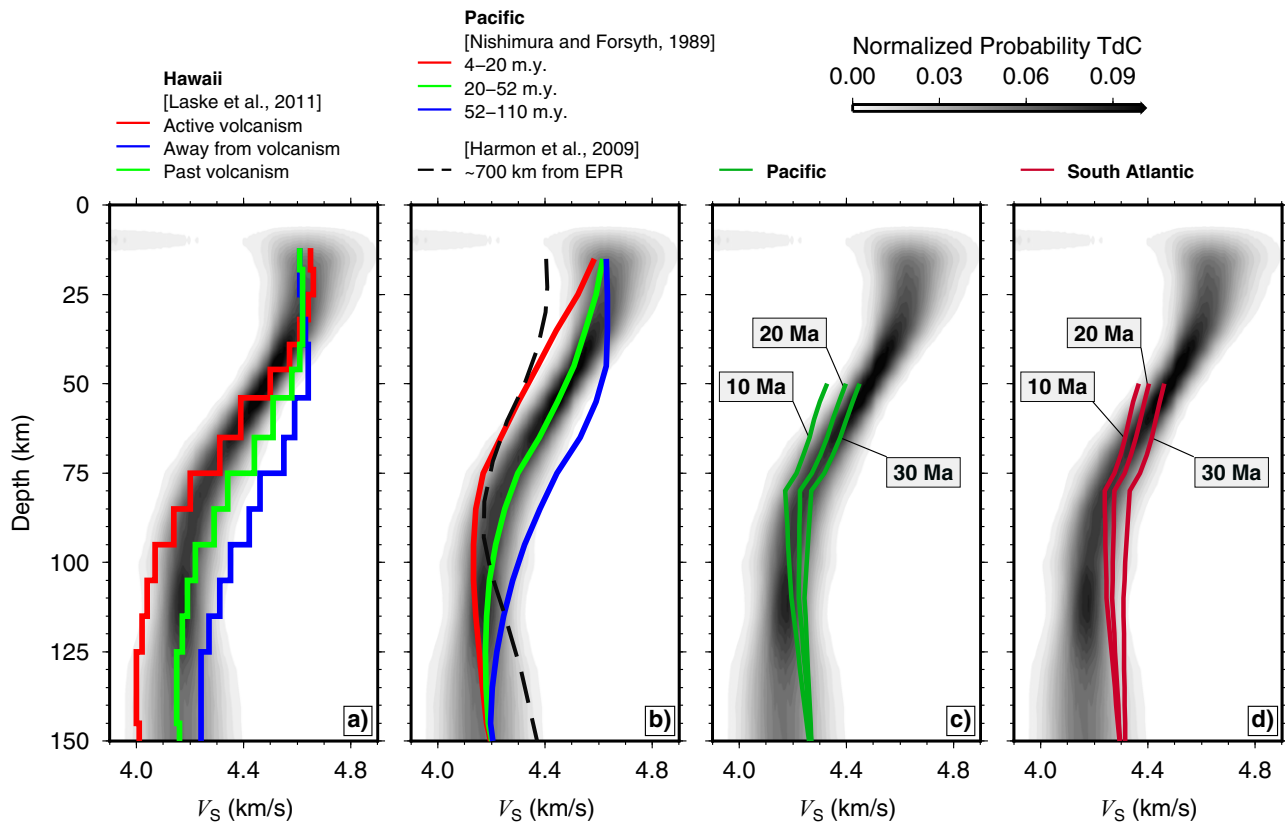
Figure 9. Comparison of our probabilistic shear-velocity profile for the TdC region (gray color scale) with V_S profiles from published models. (a) Hawaii ("Hawaii 1," "Hawaii 2," and "Hawaii 3" from Laske et al. (2011)), (b) Pacific lithosphere ("4–20 m.y.," "20–52 m.y.," and "52–110 m.y." from Nishimura and Forsyth (1989) and "∼700 km from EPR" from Harmon et al. (2009)). (c and d) Average V_S profiles for different seafloor ages in the Pacific and South Atlantic Oceans, respectively, according to global tomography (Celli et al., 2016).

had a broader period range, including periods longer than 60 s). The Hawaii profiles of Laske et al. (2011) (Figure 9a) show clearly the rejuvenation of the old Pacific lithosphere by the Hawaii hotspot. The measure of the rejuvenation is the difference between the fastest profile (blue; Pacific lithosphere unaffected by the hotspot) and the slowest profile (red; Pacific lithosphere affected by the hotspot most recently). In the lithospheric depth range, shear wave velocities beneath TdC are remarkably similar to those in the rejuvenated lithosphere beneath Hawaii ("location 1" in Laske et al. (2011), red curve in Figure 9a). Below 80–90 km depth, however, velocities in the asthenosphere beneath Tristan (4.1–4.2 km/s) are not as low as the lowest velocities beneath Hawaii (4.0 km/s). This suggests that the asthenosphere beneath Hawaii is considerably hotter than beneath Tristan (and, possibly, has more partial melt). The similarity of V_S (and, by inference, temperature) in the lithosphere beneath Tristan and Hawaii is consistent with the Hawaiian asthenosphere being much hotter. Before the rejuvenation by the hotspot, the older Pacific lithosphere must have been colder and thicker. Thus, it had to be reheated by a substantially greater amount than the younger Atlantic lithosphere beneath Tristan, for the two to have similar lithospheric geotherms at present.

Our TdC V_S profile is similar to the profiles from Nishimura and Forsyth (1989) for young and intermediate-age (4–20 and 20–52 Ma, respectively) Pacific lithosphere (Figure 9b). In the shallow lithosphere, all the profiles, including ours and those from Laske et al. (2011) and Nishimura and Forsyth (1989), agree in that V_S reaches around 4.6 km/s. This similarity is because temperature in the shallow lithosphere, which is close to the surface and cools quickly after the plate is formed, should be similar for different lithospheric ages, even though the geotherms for the different ages diverge at greater depths, in the deep lithosphere-asthenosphere depth range. Because the profiles of Nishimura and Forsyth (1989) are for isotropic-average V_S, obtained from both Love and Rayleigh-wave measurements, whereas our profile is for V_{SV}, obtained from Rayleigh waves only, we refrain from a quantitative comparison of the entire profiles, as radial anisotropy could bias any inferences. Interestingly, the model of Harmon et al. (2009) for a location around

700 km west from the East Pacific Rise (EPR), with the seafloor age of around 8 m.y., shows lower V_S in the uppermost mantle compared to the other profiles (Figure 9b). This suggests slow cooling of the Pacific lithosphere at this location. This can be attributed to the proximity of hotspots a little further west, with the profile located just between the hotspots and the ridge.

In Figures 9c and 9d, we compare our Tristan profile with V_S profiles computed as averages for different lithospheric ages within the South Atlantic and Pacific Oceans, using a global tomographic model (Celli et al., 2016). The global tomography shows that V_{SV} in the asthenosphere beneath the South Atlantic is higher than beneath the Pacific Ocean, on average. Shear velocity in the asthenosphere beneath the Tristan region, according to the profile obtained in this study, is lower than the South Atlantic average for the corresponding age range (10–30 m.y.), obtained from the tomography. This confirms that the asthenosphere beneath Tristan is anomalously warm.

5.2. Estimation of Temperature From V_S Profile

An alternative, independent quantitative estimate of the temperature anomaly beneath TdC can be obtained by using our V_S profile and published, petrologically derived $V_S - T$ relationships (e.g., Goes et al., 2012). Converting seismic information to temperature is complicated by the large number of variables involved (temperature, pressure, composition, phase, melt content, water content, attenuation) and by uncertainties in the available thermodynamic databases. Goes et al. (2012) used three different published attenuation (Q) models specifically to relate the low velocity anomalies in the mantle below mid-ocean ridges to temperature anomalies. Taking into account anharmonic and anelastic effects of temperature, pressure, composition, phase and water content, they computed V_S profiles for the different Q models; the first one a model from Behn et al. (2009) based on the results of Faul and Jackson (2005) and Jackson et al. (2002), the second one an empirical model from Goes et al. (2000) and van Wijk et al. (2008), and the third one a model proposed by Yang et al. (2007) (we refer to the models as Q_F, Q_g, and Q_Y, maintaining the notation from Goes et al. (2012) (e.g., their Figure 4)).

We estimated temperatures using $V_S - T$ relationships from Goes et al. (2012) (e.g., their Figure 4). Assuming σ and 2σ uncertainties on the posterior V_S distribution yielded by our probabilistic inversion, we obtained the ranges of temperature at 50, 75 and 100 km shown in Table 1. The $V_S - T$ relationships were recomputed at a reference period of 50 s (which is the reference period we use in our inversion). In order to obtain the estimates at 75 km, we interpolated logarithmically between 50 and 100 km. The resulting temperature values are also shown in Figure 10, where we compare them with our petrological models and other models. At 50 km, Q_F produces the highest temperature estimate and Q_Y the lowest; the opposite is true at 100 km. The 2σ error bars in Figure 10 differ in width because of the different frequency dependence of the three models. At 50 km depth, all three estimates are close to temperatures in our petrologically derived models (green and red lines in Figure 10). At 75 and 100 km, our petrologically derived geotherms are in agreement with Q_g and Q_Y, but not Q_F. The two attenuation models that are consistent with the petrologically derived geotherms, Q_g and Q_Y, are both empirical, the first one designed to reconcile a wide range of observations and the second one to fit EPR attenuation (see Goes et al. (2012) for details). Q_F, in contrast, is a model based on laboratory results only. (We note that recent experimental updates from Jackson and Faul (2010) (following Faul and Jackson (2005)) would suggest higher predicted moduli (higher velocity and less attenuation) at a given temperature.)

Table 1
Estimation of Temperature Using Our Average V_S Model and $V_S - T$ Relationships From Goes et al. (2012*) at Three Different Depths and for Three Different Attenuation Models,* Q_F, Q_g, *and* Q_Y

Depth (km)		T_σ (°C)	$T_{2\sigma}$ (°C)
50	Q_F	$1,006 \pm 41$	989 ± 93
	Q_g	958 ± 47	946 ± 96
	Q_Y	866 ± 65	852 ± 141
75	Q_F	$1,223 \pm 38$	$1,213 \pm 79$
	Q_g	$1,239 \pm 52$	$1,230 \pm 109$
	Q_Y	$1,228 \pm 95$	$1,231 \pm 190$
100	Q_F	$1,310 \pm 30$	$1,304 \pm 63$
	Q_g	$1,391 \pm 48$	$1,384 \pm 96$
	Q_Y	$1,423 \pm 93$	$1,419 \pm 195$

5.3. Synthesis: Thickness of the Lithosphere and Temperature of the Asthenosphere

We summarize the evidence on the seismic and thermal structures of the lithosphere-asthenosphere system beneath TdC in Figure 10. In Figure 10a, TdC V_S probability distribution is compared to a recent V_S model for the rejuvenated lithosphere beneath Hawaii from Laske et al. (2011). Our model shows a pronounced low-velocity anomaly from ∼70 to at least ∼120 km depth with S wave velocity in the low-velocity zone around 4.1–4.2 km/s, higher than beneath Hawaii (∼4.0 km/s). The Pacific lithosphere beneath the eastern extremity of the Hawaii chain, where volcanism is now active, is 90–100 Ma,
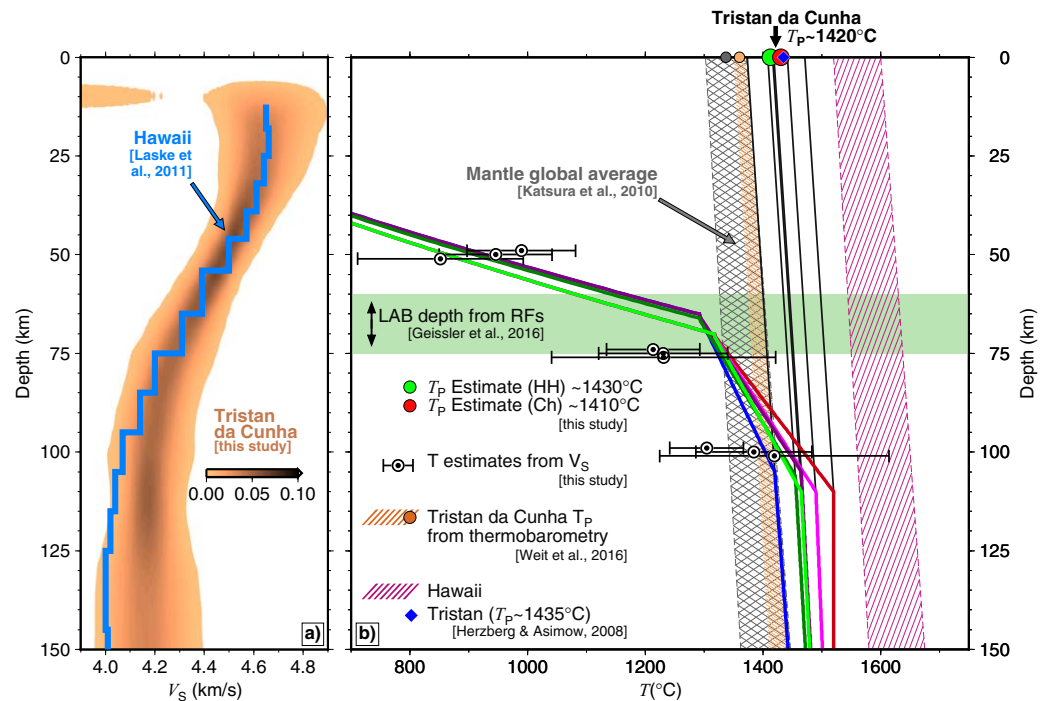
Figure 10. Synthesis of the key evidence on the thermal structure of the upper mantle beneath Tristan da Cunha. (a) The lithosphere beneath TdC is underlain by a pronounced low-velocity zone, indicative of anomalously warm asthenosphere. However, V_S in the TdC asthenosphere is not as low as beneath Hawaii (Laske et al., 2011), which suggests that the thermal anomaly beneath TdC is not as high as that beneath Hawaii. (b) The petrologically derived models that are consistent with seismic and bathymetry data (dark/light green and dark/light purple lines—models 5, 6, 4, and 3 according to the legend at the top right corner in Figure 8) have the LAB at a depth of 65–70 km, in agreement with the LAB depths computed from receiver functions (Geissler et al., 2016) (light green band). These models suggest a mantle potential temperature T_P beneath Tristan of 1,410–1,430°C, higher than the global average (~1,337 ± 35°C (Katsura et al., 2010)) but lower than at the Hawaii hotspot (~1,520–1,600°C, according to Herzberg and Asimow (2008)). Our estimated potential temperature for TdC is close to the value computed for Tristan by Herzberg and Asimow (2008) (~1,435°C, blue diamond). The coldest and hottest petrological models (dark blue and dark red, respectively) are not consistent with seismic data. "HH" and "Ch" indicate if the model has been computed using the parameterization from Hammond and Humphreys (2000a, 2000b) or Chantel et al. (2016), respectively (see also the legend in Figure 8). We also plot the T_P recently inferred from thermobarometry (Weit et al., 2016) (~1,360°C; orange circle and band). The temperature estimates from our V_S and the $V_S - T$ relationships of Goes et al. (2012) (Table 1) are plotted as circles with error bars. These temperature estimates are computed for three different attenuation models, all at the depths of 50, 75, and 100 km; they are plotted at slightly different depths (±1 km) for clarity. The (conservatively broad) geothermal gradient range used to relate T_P and the temperature in the asthenosphere is [0.4, 0.5] K/km (Katsura et al., 2010).

substantially older than the 10–30 My age of the lithosphere beneath the TdC region. The similarity of the lithospheric V_S profiles from the two locations thus indicates that the Hawaii hotspot has warmed and thinned the Pacific lithosphere by a much greater amount (seen in the comparison of the Hawaii-region profiles in Figure 9a) than the Tristan hotspot has the South Atlantic lithosphere. This is consistent with the asthenosphere beneath TdC being not nearly as hot as it is beneath Hawaii, as indicated by the higher V_S in the TdC asthenosphere.

Petrological modeling shows that the seismic and bathymetric data from the TdC region can be fit by models with a moderately hot mantle, a melt fraction smaller than 1% and a 65–70 km lithospheric thickness (in agreement with the purely seismic inversions). Figure 10b compares the well-fitting, petrologically derived geotherms with other estimates for TdC, with the global average and with estimates for Hawaii. The mantle-adiabatic temperature gradient range used to relate the temperatures in the asthenosphere to the mantle potential temperature T_P is 0.4–0.5 K/km (taken from Katsura et al. (2010)). We also show the lithospheric thickness inferred from receiver functions (Geissler et al., 2016) and temperature estimates (section 5.2) from V_S profile and $V_S - T$ relationships (Goes et al., 2012).

Our results show that the TdC mantle is warmer than ambient mantle beneath normal ocean ridges: T_P of 1,410–1,430°C for Tristan versus 1,280–1,400°C (Anderson, 2000; Chambers et al., 2005; Herzberg et al., 2007; Katsura et al., 2010; Khan et al., 2013; Kuskov et al., 2014) for the ridges. Our potential temperature estimates are higher than the values calculated by Dalton et al. (2014) on the MAR for the closest locations to Tristan da Cunha (1,349°C, 1,367°C, 1,393°C, and 1,378°C at the values of latitude-longitude [−40, −16], [−38, −17], [−36, −17], and [−35, −15], respectively). This thermal anomaly is considerably smaller than anomalies beneath some of the other major hotspots (Hawaii, 1,520–1,600°C (Herzberg & Asimow, 2008; Herzberg et al., 2007; Taposeea et al., 2016); Samoa, ∼1,525°C; St. Helena, ∼1,520°C (Herzberg & Asimow, 2008)), but it is in the range of estimates reported for other hotspots (Iceland, 1,435–1,455°C; Azores, 1,430–1,465°C; Canaries, 1,420–1,480°C (Herzberg & Asimow, 2008)). (The overall higher values reported by Putirka (2005, 2008) and Putirka et al. (2007) also show Hawaii (1,687–1,722°C) to be hotter than Iceland (1,583–1,637°C).) Our estimated T_P for TdC is close to the value estimated for Tristan by Herzberg and Asimow (2008) (∼1,435°C). The temperature beneath Tristan, according to our models, is about 50–120°C higher than the global average value of 1,337 ± 35°C (Katsura et al., 2010).

6. Conclusions

Rayleigh-wave dispersion measurements from OBS data in the Tristan da Cunha region reveal a 65–70 km thick lithosphere and a pronounced low-velocity zone beneath 70 km depth, with V_S of 4.1–4.2 km/s within it. Both the probabilistic seismic inversion of the data and petrological modeling indicate the lithospheric thickness around 65–70 km, which agrees with independent estimates from receiver functions (Geissler et al., 2016). The temperature of the asthenosphere is around 50–120°C higher than global average, with a melt fraction smaller than 1%. The mantle potential temperature T_P is estimated at about 1,410–1,430°C.

Our observations are consistent with a hot upwelling from the deep mantle (a mantle plume) beneath the Tristan region, but the excess temperature we determine is smaller than that reported for some major hotspots such as Hawaii (100–180°C), although it is in the range of values reported for Iceland and some other hotspots. The upwelling beneath TdC may be not as hot as that beneath Hawaii or, alternatively, the present structure reflects a weaker upwelling (plume tail) than in the past, when the large igneous provinces onshore and the prominent hotspot tracks offshore were formed. It is also possible that the largest thermal anomaly is located at a distance from TdC, closer to the MAR (Figure 1b).

References

Afonso, J. C., Fernández, M., Ranalli, G., Griffin, W. L., & Connolly, J. A. D. (2008). Integrated geophysical-petrological modeling of the lithosphere and sublithospheric upper mantle: Methodology and applications. *Geochemistry, Geophysics, Geosystems*, 9, Q05008. https://doi.org/10.1029/2007GC001834

Agius, M., & Lebedev, S. (2014). Shear-velocity structure, radial anisotropy and dynamics of the Tibetan crust. *Geophysical Journal International*, 199(3), 1395–1415.

Agius, M. R., & Lebedev, S. (2013). Tibetan and Indian lithospheres in the upper mantle beneath Tibet: Evidence from broadband surface-wave dispersion. *Geochemistry, Geophysics, Geosystems*, 14, 4260–4281. https://doi.org/10.1002/ggge.20274

Anderson, D. (2005). Scoring hotspots: The plume and plate paradigms. *Geological Society of America Special Papers*, 388, 31–54.

Anderson, D. L. (2000). The thermal state of the upper mantle: No role for mantle plumes. *Geophysical Research Letters*, 27(22), 3623–3626.

Baba, K., Chen, J., Sommer, M., Utada, H., Geissler, W. H., Jokat, W., et al. (2017). Marine magnetotellurics imaged no distinct plume beneath the Tristan da Cunha hotspot in the southern Atlantic Ocean. *Tectonophysics*, 716, 52–63.

Bartzsch, S., Lebedev, S., & Meier, T. (2011). Resolving the lithosphere-asthenosphere boundary with seismic Rayleigh waves. *Geophysical Journal International*, 186(3), 1152–1164.

Bassin, C., Laske, G., & Masters, G. (2000). The current limits of resolution for surface wave tomography in North America. *Eos, Transactions American Geophysical Union*, 81, F897.

Behn, M. D., Hirth, G., & Elsenbeck, G. R. II (2009). Implications of grain size evolution on the seismic structure of the oceanic upper mantle. *Earth and Planetary Science Letters*, 282(1–4), 178–189.

Bodin, T., Leiva, J., Romanowicz, B., Maupin, V., & Yuan, H. (2016). Imaging Anisotropic layering with Bayesian inversion of multiple data types. *Geophysical Journal International*, 206(1), 605–629. https://doi.org/10.1093/gji/ggw124

Bodin, T., Sambridge, M., Tkalcic, H., Arroucau, P., Gallagher, K., & Rawlinson, N. (2012). Transdimensional inversion of receiver functions and surface wave dispersion. *Journal of Geophysical Research*, 117, B02301. https://doi.org/10.1029/2011JB008560

Celli, N. L., Lebedev, S., Schaeffer, A., & Gaina, C. (2016). Waveform tomography of the South Atlantic Region. *Fall Meeting Conference Abstract*. Washington, DC: American Geophysical Union.

Chambers, K., Woodhouse, J., & Deuss, A. (2005). Topography of the 410-km discontinuity from PP and SS precursors. *Earth and Planetary Science Letters*, 235(3–4), 610–622.

Chantel, J., Manthilake, G., Andrault, D., Novella, D., Yu, T., & Wang, Y. (2016). Experimental evidence supports mantle partial melting in the asthenosphere. *Science Advances*, 2(5), e1600246. https://doi.org/10.1126/sciadv.1600246

Connolly, J. A. D. (2005). Computation of phase equilibria by linear programming: A tool for geodynamic modeling and its application to subduction zone decarbonation. *Earth and Planetary Science Letters*, *236*(1–2), 524–541. https://doi.org/10.1016/j.epsl.2005.04.033

Courtillot, V., Davaille, A., Besse, J., & Stock, J. (2003). Three distinct types of hotspots in the Earth's mantle. *Earth and Planetary Science Letters*, *205*(3–4), 295–308. https://doi.org/10.1016/S0012-821X(02)01048-8

Dalton, C. A., Langmuir, C. H., & Gale, A. (2014). Geophysical and geochemical evidence for deep temperature variations beneath mid-ocean ridges. *Science*, *344*(6179), 80, https://doi.org/10.1126/science.1249466

Deschamps, F., Lebedev, S., Meier, T., & Trampert, J. (2008). Azimuthal anisotropy of Rayleigh-wave phase velocities in the east-central United States. *Geophysical Journal International*, *173*(3), 827–843.

Dziewonski, A. M., & Anderson, D. L. (1981). Preliminary reference Earth model. *Physics of the Earth and Planetary Interiors*, *25*(4), 297–356.

Dziewonski, A. M., Chou, T.-A., & Woodhouse, J. H. (1981). Determination of earthquake source parameters from waveform data for studies of global and regional seismicity. *Journal of Geophysical Research*, *86*(B4), 2825–2852. https://doi.org/10.1029/JB086iB04p02825

Ekström, G., Nettles, M., & Dziewoński, A. M. (2012). The global CMT project 2004–2010: Centroid-moment tensors for 13017 earthquakes. *Physics of the Earth and Planetary Interiors*, *200–201*, 1–9.

Endrun, B., Lebedev, S., Meier, T., Tirel, C., & Friederich, W. (2011). Complex layered deformation within the Aegean crust and mantle revealed by seismic anisotropy. *Nature Geoscience*, *4*(3), 203–207.

Erduran, M., Endrun, B., & Meier, T. (2008). Continental vs. oceanic lithosphere beneath the eastern Mediterranean Sea—Implications from Rayleigh wave dispersion measurements. *Tectonophysics*, *457*(1–2), 42–52.

Fairhead, J., & Wilson, M. (2005). Plate tectonic processes in the South Atlantic Ocean: Do we need deep mantle plumes? *Geological Society of America Special Papers*, *388*, 537–553.

Faul, U. H., & Jackson, I. (2005). The seismological signature of temperature and grain size variations in the upper mantle. *Earth and Planetary Science Letters*, *234*(1–2), 119–134.

Foulger, G., & Natland, J. H. (2003). Is ''hotspot'' volcanism a consequence of plate tectonics? *Science*, *300*(5621), 921–922.

French, S., & Romanowicz, B. (2015). Broad plumes rooted at the base of the Earth's mantle beneath major hotspots. *Nature*, *525*(7567), 95–99. https://doi.org/10.1038/nature14876

Fullea, J., Afonso, J. C., Connolly, J. A. D., Fernandez, M., Garcia-Castellanos, D., & Zeyen, H. (2009). LitMod3D: An interactive 3-D software to model the thermal, compositional, density, seismological, and rheological structure of the lithosphere and sublithospheric upper mantle. *Geochemistry, Geophysics, Geosystems*, *10*, Q08019. https://doi.org/10.1029/2009GC002391

Fullea, J., Camacho, A. G., Negredo, A. M., & Fernández, J. (2015). The Canary Islands hotspot: New insights from 3D coupled geophysical-petrological modelling of the lithosphere and uppermost mantle. *Earth and Planetary Science Letters*, *409*, 71–88.

Fullea, J., Lebedev, S., Agius, M., Jones, A., & Afonso, J. (2012). Lithospheric structure in the Baikal-central Mongolia region from integrated geophysical-petrological inversion of surface-wave data and topographic elevation. *Geochemistry, Geophysics, Geosystems*, *13*, Q0AK09. https://doi.org/10.1029/2012GC004138

Gassmöller, R., Dannberg, J., Bredow, E., Steinberger, B., & Torsvik, T. H. (2016). Major influence of plume-ridge interaction, lithosphere thickness variations, and global mantle flow on hotspot volcanism—The example of Tristan. *Geochemistry, Geophysics, Geosystems*, *17*, 1454–1479. https://doi.org/10.1002/2015GC006177

Geissler, W. (2014). Electromagnetic, gravimetric and seismic measurements to investigate the Tristan da Cunha hotspot and its role in the opening of the South Atlantic Ocean (MARKE)—Cruise No. MSM24—December 27, 2012—January 21, 2013—Walvis Bay (Namibia)—Cape Town (South Africa), 1–56, MARIA S. MERIAN-Berichte, MSM24. ISSN 2195–8483. https://doi.org/10.2312/cr_msm24

Geissler, W. H., Jokat, W., Jegen, M., & Baba, K. (2016). Thickness of the oceanic crust, the lithosphere, and the mantle transition zone in the vicinity of the Tristan da Cunha hotspot estimated from ocean-bottom and ocean-island seismometer receiver functions. *Tectonophysics*, *716*, 33–51. https://doi.org/10.1016/j.tecto.2016.12.013

Gibson, S., Thompson, R., & Day, J. (2006). Timescales and mechanisms of plume-lithosphere interactions: ^{40}Ar/^{39}Ar geochronology and geochemistry of alkaline igneous rocks from the Paraná-Etendeka large igneous province. *Earth and Planetary Science Letters*, *251*(1–2), 1–17. https://doi.org/10.1016/j.epsl.2006.08.004

Godfrey, K. E., Dalton, C. A., & Ritsema, J. (2017). Seafloor age dependence of Rayleigh wave phase velocities in the Indian Ocean. *Geochemistry, Geophysics, Geosystems*, *18*, 1926–1942. https://doi.org/10.1002/2017GC006824

Goes, S., Armitage, J., Harmon, N., Smith, H., & Huismans, R. (2012). Low seismic velocities below mid-ocean ridges: Attenuation versus melt retention. *Journal of Geophysical Research*, *117*, B12403. https://doi.org/10.1029/2012JB009637

Goes, S., Govers, R., & Vacher, P. (2000). Shallow mantle temperatures under Europe from P and S wave tomography. *Journal of Geophysical Research*, *105*(B5), 11153–11169. https://doi.org/10.1029/1999JB900300

Hammond, W. C., & Humphrey, E. D. (2000a). Upper mantle seismic wave velocity: Effects of realistic partial melt geometries. *Journal of Geophysical Research*, *105*(B5), 10,975–10,986.

Hammond, W. C., & Humphrey, E. D. (2000b). Upper mantle seismic wave attenuation: Effects of realistic partial melt distribution. *Journal of Geophysical Research*, *105*(B5), 10,987–10,999.

Harmon, N., Forsyth, D. W., & Weeraratne, D. S. (2009). Thickening of young Pacific lithosphere from high-resolution Rayleigh wave tomography: A test of the conductive cooling model. *Earth and Planetary Science Letters*, *278*(1–2), 96–106.

Herzberg, C., Asimow, P., Arndt, N., Niu, Y., Lesher, C., Fitton, J., et al. (2007). Temperatures in ambient mantle and plumes: Constraints from basalts, picrites, and komatiites. *Geochemistry, Geophysics, Geosystems*, *8*, Q02006. https://doi.org/10.1029/2006GC001390

Herzberg, C., & Asimow, P. D. (2008). Petrology of some oceanic island basalts: PRIMELT2.XLS software for primary magma calculation. *Geochemistry, Geophysics, Geosystems*, *9*, Q09001. https://doi.org/10.1029/2008GC002057

Humphris, S. E., Thompson, G., Schilling, J.-G., & Kingsley, R. H. (1985). Petrological and geochemical variations along the Mid-Atlantic Ridge between 46 s and 32 s: Influence of the Tristan da Cunha mantle plume. *Geochimica et Cosmochimica Acta*, *49*(6), 1445–1464.

Jackson, I., & Faul, U. H. (2010). Grainsize-sensitive viscoelastic relaxation in olivine: Towards a robust laboratory-based model for seismological application. *Physics of the Earth and Planetary Interiors*, *183*(1–2), 151–163.

Jackson, I., Fitz Gerald, J. D., Faul, U. H., & Tan, B. H. (2002). Grain-size-sensitive seismic wave attenuation in polycrystalline olivine. *Journal of Geophysical Research*, *107*(B12), 2360. https://doi.org/10.1029/2001JB001225

James, E. K., Dalton, C. A., & Gaherty, J. B. (2014). Rayleigh wave phase velocities in the Atlantic upper mantle. *Geochemistry, Geophysics, Geosystems*, *15*, 4305–4324. https://doi.org/10.1002/2014GC005518

Katsura, T., Yoneda, A., Yamazaki, D., Yoshino, T., & Ito, E. (2010). Adiabatic temperature profile in the mantle. *Physics of the Earth and Planetary Interiors*, *183*(1–2), 212–218.

Katz, R., Spiegelman, M., & Langmuir, C. H. (2003). A new parameterization of hydrous mantle melting. *Geochemistry, Geophysics, Geosystems*, *4*, 1073. https://doi.org/10.1029/2002GC000433

Kennett, B., Engdahl, E., & Buland, R. (1995). Constraints on seismic velocities in the Earth from traveltimes. *Geophysical Journal International*, *122*(1), 108–124.

Khan, A., Zunino, A., & Deschamps, F. (2013). Upper mantle compositional variations and discontinuity topography imaged beneath Australia from Bayesian inversion of surface-wave phase velocities and thermochemical modeling. *Journal of Geophysical Research: Oceans*, *118*, 5285. https://doi.org/10.1002/jgrb50304

Kuskov, O., Kronrod, V., Prokofyev, A., & Pavlenkova, N. (2014). Thermo-chemical structure of the lithospheric mantle underneath the Siberian craton inferred from long-range seismic profiles. *Tectonophysics*, *615–616*, 154–166.

Laske, G., Markee, A., Orcutt, J. A., Wolfe, C. J., Collins, J. A., Solomon, S. C., et al. (2011). Asymmetric shallow mantle structure beneath the Hawaiian Swell—Evidence from Rayleigh waves recorded by the PLUME network. *Geophysical Journal International*, *187*, B12403. https://doi.org/10.1111/j.1365-246X.2011.05238.x

Lebedev, S., Adam, J. M.-C., & Meier, T. (2013). Mapping the Moho with seismic surface waves: A review, resolution analysis, and recommended inversion strategies. *Tectonophysics*, *609*, 377–394.

Lebedev, S., Meier, T., & van der Hilst, R. D. (2006). Asthenospheric flow and origin of volcanism in the Baikal Rift area. *Earth and Planetary Science Letters*, *249*(3–4), 415–424.

Lebedev, S., & van der Hilst, R. D. (2008). Global upper-mantle tomography with the automated multimode inversion of surface and S-wave forms. *Geophysical Journal International*, *173*(2), 505–518.

Lindquist, K. G., Engle, K., Stahlke, D., & Price, E. (2004). Global topography and bathymetry grid improves research efforts. *Eos, Transactions American Geophysical Union*, *85*(19), 186.

Meier, T., Dietrich, K., Stockhert, B., & Harjes, H. (2004). One-dimensional models of shear wave velocity for the eastern Mediterranean obtained from the inversion of Rayleigh wave phase velocities and tectonic implications. *Geophysical Journal International*, *156*(1), 45–58. https://doi.org/10.1111/j.1365-246X.2004.02121.x

Morgan, J. P. (1997). The generation of a compositional lithosphere by mid-ocean ridge melting and its effect on the subsequent off-axis hotspot upwelling and melting. *Earth and Planetary Science Letters*, *146*, 213–232.

Morgan, W. J. (1971). Convection plumes in the lower mantle. *Nature*, *230*(5288), 42–43.

Nishimura, C. E., & Forsyth, D. W. (1989). The anisotropic structure of the upper mantle in the Pacific. *Geophysical Journal*, *96*(2), 203–229.

NOAA, N. G. D. C. (2006). *2-minute Gridded Global Relief Data (ETOPO2) v2*. Silver Spring, MD: National Oceanic and Atmospheric Administration. https://doi.org/10.7289/V5J1012Q

O'Connor, J. M., & Duncan, R. A. (1990). Evolution of the Walvis Ridge-Rio Grande rise hotspot system: Implications for African and South American Plate motions over plumes. *Journal of Geophysical Research*, *95*(B11), 17475–17502. https://doi.org/10.1029/JB095iB11p17475

O'Connor, J. M., & Jokat, W. (2015). Tracking the Tristan-Gough mantle plume using discrete chains of intraplate volcanic centers buried in the Walvis Ridge. *Geology*, *3*(8), 715–718. https://doi.org/10.1130/G36767.1

O'Connor, J. M., Jokat, W., Le Roex, A., Class, C., Wijbrans, J., Keszling, S., et al. (2012). Hotspot trails in the South Atlantic controlled by plume and plate tectonic processes. *Nature Geoscience*, *5*(10), 735–738.

Pawlak, A., Eaton, D. W., Darbyshire, F., Lebedev, S., & Bastow, I. D. (2012). Crustal anisotropy beneath Hudson Bay from ambient noise tomography: Evidence for post-orogenic lower-crustal flow? *Journal of Geophysical Research*, *117*, B08301. https://doi.org/10.1029/2011JB009066

Polat, G., Lebedev, S., Readman, P. W., O'Reilly, B. M., & Hauser, F. (2012). Anisotropic Rayleigh-wave tomography of Ireland's crust: Implications for crustal accretion and evolution within the Caledonian Orogen. *Geophysical Research Letters*, *39*, L04302. https://doi.org/10.1029/2012GL051014

Putirka, K. (2008). Excess temperatures at ocean islands: Implications for mantle layering and convection. *Geology*, *36*(4), 283–286. https://doi.org/10.1130/G24615A.1

Putirka, K. D. (2005). Mantle potential temperatures at Hawaii, Iceland, and the mid-ocean ridge system, as inferred from olivine phenocrysts: Evidence for thermally driven mantle plumes. *Geochemistry, Geophysics, Geosystems*, *6*, Q05L08. https://doi.org/10.1029/2005GC000915

Putirka, K. D., Perfit, M., Ryerson, F. J., & Jackson, M. J. (2007). Ambient and excess mantle temperatures, olivine thermometry, and active vs. passive upwelling. *Chemical Geology*, *241*(3–4), 177–206.

Ravenna, M., & Lebedev, S. (2018). Bayesian inversion of surface-wave data for radial and azimuthal shear-wave anisotropy, with applications to central Mongolia and west-central Italy. *Geophysical Journal International*, *213*(1), 278–300. https://doi.org/10.1093/gji/ggx497

Rawlinson, N., Arroucau, P., Musgrave, R., Cayley, R., Young, M., & Salmon, M. (2014). Complex continental growth along the proto-Pacific margin of East Gondwana. *Geology*, *42*(9), 783–786. https://doi.org/10.1130/G35766.1

Rohde, J., Hoernle, K., Hauff, F., Werner, R., O'connor, J., Class, C., et al. (2013). 70 Ma chemical zonation of the Tristan-Gough hotspot track. *Geology*, *41*(3), 335–338. https://doi.org/10.1130/G33790.1

Rohde, J. K., van den Bogaard, P., Hoernle, K., Hauff, F., & Werner, R. (2013). Evidence for an age progression along the Tristan-Gough volcanic track from new $^{40}Ar/^{39}Ar$ ages on phenocryst phases. *Tectonophysics*, *604*, 60–71. https://doi.org/10.1016/j.tecto.2012.08.026

Roux, E., Moorkamp, M., Jones, A., Bischoff, M., Endrun, B., Lebedev, S., et al. (2011). Joint inversion of long-period magnetotelluric data and surface-wave dispersion curves for anisotropic structure: Application to data from Central Germany. *Geophysical Research Letters*, *38*, L05304. https://doi.org/10.1029/2010GL046358

Ryberg, T., Geissler, W., Jokat, W., & Pandey, S. (2017). Uppermost mantle and crustal structure at Tristan da Cunha derived from ambient seismic noise. *Earth and Planetary Science Letters*, *471*, 117–124.

Schaeffer, A. J., & Lebedev, S. (2013). Global shear speed structure of the upper mantle and transition zone. *Geophysical Journal International*, *194*(1), 417–449.

Schaeffer, A. J., & Lebedev, S. (2015). Global heterogeneity of the lithosphere and underlying mantle: A seismological appraisal based on multimode surface-wave dispersion analysis, shear-velocity tomography, and tectonic regionalization (Invited Review). In Khan, A. & Deschamps, F. (Eds.), *The Earth's heterogeneous mantle, Springer Geophysics* (pp. 3–46). Berlin, Germany: Springer. https://doi.org/10.1007/978-3-319-15627-9

Schlömer, A., Geissler, W. H., Jokat, W., & Jegen, M. (2017). Hunting for the Tristan mantle plume—An upper mantle tomography around the volcanic island of Tristan da Cunha. *Earth and Planetary Science Letters*, *462*, 122–131.

Sens-Schönfelder, C. (2008). Synchronizing seismic networks with ambient noise. *Geophysical Journal International*, *174*(3), 966–970.

Soomro, R., Weidle, C., Cristiano, L., Lebedev, S., & Meier, T. (2016). Phase velocities of Rayleigh and Love waves in central and northern Europe from automated, broadband, inter-station measurements. *Geophysical Journal International*, *204*(1), 517–534. https://doi.org/10.1093/gji/ggv462

Takei, Y. (2017). Effects of partial melting on seismic velocity and attenuation: A new insight from experiments. *Annual Review of Earth and Planetary Sciences*, *45*(1), 447–470. https://doi.org/10.1146/annurev-earth-063016-015820

Taposeea, C. A., Armitage, J. J., & Collier, J. S. (2016). Asthenosphere and lithosphere structure controls on early onset oceanic crust production in the southern South Atlantic. *Tectonophysics*, *716*, 4–20. https://doi.org/10.1016/j.tecto.2016.06.026

van Wijk, J., van Hunen, J., & Goes, S. (2008). Small-scale convection during continental rifting: Evidence from the Rio Grande rift. *Geology*, *36*(7), 575–578. https://doi.org/10.1130/G24691A.1

Weit, A., Trumbull, R., Keiding, J., Geissler, W., Gibson, S., & Veksler, I. (2016). The magmatic system beneath the Tristan da Cunha hotspot: Insights from thermobarometry, melting models and geophysics. *Tectonophysics*, *716*, 64–76. https://doi.org/10.1016/j.tecto.2016.08.010

Wessel, P., Smith, W. H. F., Scharroo, R., Luis, J., & Wobbe, F. (2013). Generic mapping tools: Improved version released. *Eos, Transactions American Geophysical Union*, *94*(45), 409–420.

Yamauchi, H., & Takei, Y. (2016). Polycrystal anelasticity at near-solidus temperatures. *Journal of Geophysical Research: Solid Earth*, *121*, 7790–7820. https://doi.org/10.1002/2016JB013316

Yang, Y., Forsyth, D. W., & Weeraratne, D. S. (2007). Seismic attenuation near the East Pacific Rise and the origin of the low-velocity zone. *Earth and Planetary Science Letters*, *258*(1–2), 260–268.

Zhang, Y.-S., & Tanimoto, T. (1993). High-resolution global upper mantle structure and plate tectonics. *Journal of Geophysical Research*, *98*(B6), 9793–9823. https://doi.org/10.1029/93JB00148